J. Fluid Mech. (1972), *vol.* 54, *part* 2, *pp.* 241–261
Printed in Great Britain

The mechanics of an organized wave in turbulent shear flow. Part 2. Experimental results

By A. K. M. F. HUSSAIN† AND W. C. REYNOLDS
Department of Mechanical Engineering, Stanford University

(Received 18 October 1971)

Results on the behaviour of controlled wave disturbances introduced artificially into turbulent channel flow are reported. Weak plane-wave disturbances are introduced by vibrating ribbons near each wall. The amplitude and relative phase of the streamwise component of the induced wave is educed from a hot-wire signal, allowing the wave speed, the attenuation characteristics and the wave shape to be traced downstream. These results form a basis for evaluation of closure models for the dynamical equations describing wave components in shear-flow turbulence.

1. Recapitulation

This paper is a direct continuation of Hussain & Reynolds (1970*a*), hereafter referred to as I, and summarizes all the key experimental results given in our report Hussain & Reynolds (1970*b*), hereafter referred to as R. Connexions with theoretical models will be discussed in part 3 (Reynolds & Hussain 1972). The problem at hand is the description of the behaviour of controlled periodic (sinusoidal) disturbances artificially introduced into a turbulent channel flow. Motivations for this work are elaborated in I and R, and include the current interest in possible wave theories of turbulent shear flow (Landahl 1967).

The basic apparatus (see figure 2 of I) involves an air flow channel with a gap of 2·5 inches in which vibrating ribbons located in the flow on opposite sides of the channel are used to introduce sinusoidal disturbances of a controlled frequency and phase into fully developed two-dimensional turbulent channel flow (see figure 1). The objective is to measure the propagation and decay characteristics of disturbances of chosen frequencies, and to relate these measurements to theoretical treatments. The basic flow was described in I‡ and is documented in greater detail in R. Particular attention was paid to the elimination of residual large-scale motions arising from the entrance conditions, and the long length of this apparatus (length/gap ratio of 230) gives a degree of turbulence-structure development not previously achieved.

The ribbon vibration is produced by passing an alternating current through the ribbons, which are located in a steady magnetic field. The ribbons may be

† Present address: Department of Mechanical Engineering, University of Houston, Houston, Texas.

‡ In figure 4 of I the ordinate should be (0, 2·0) instead of (0, 20).

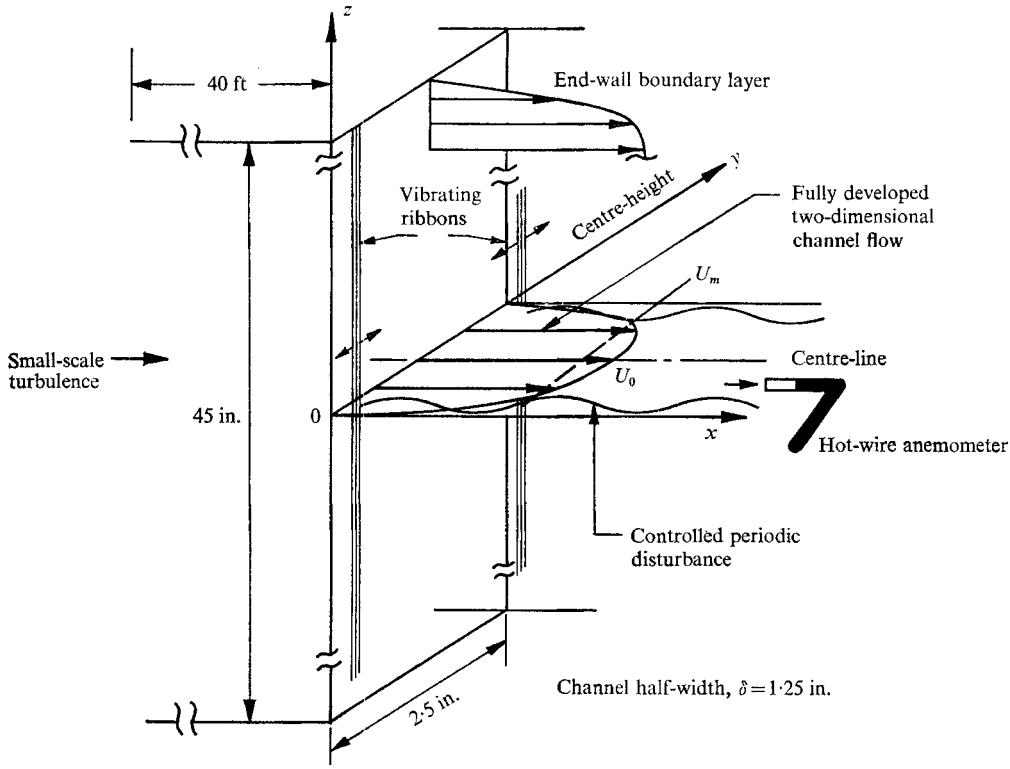

FIGURE 1. Schematic diagram of test flow.

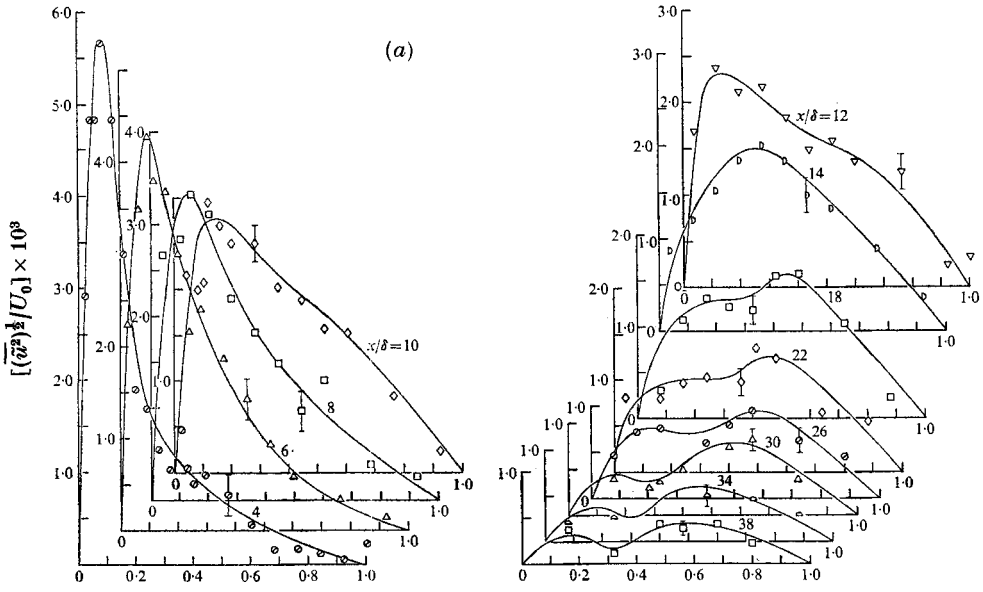

FIGURE 2. Measured (*a*) $\tilde{u}$ amplitude and (*b*) $\tilde{u}$ phase distributions at 25 Hz.

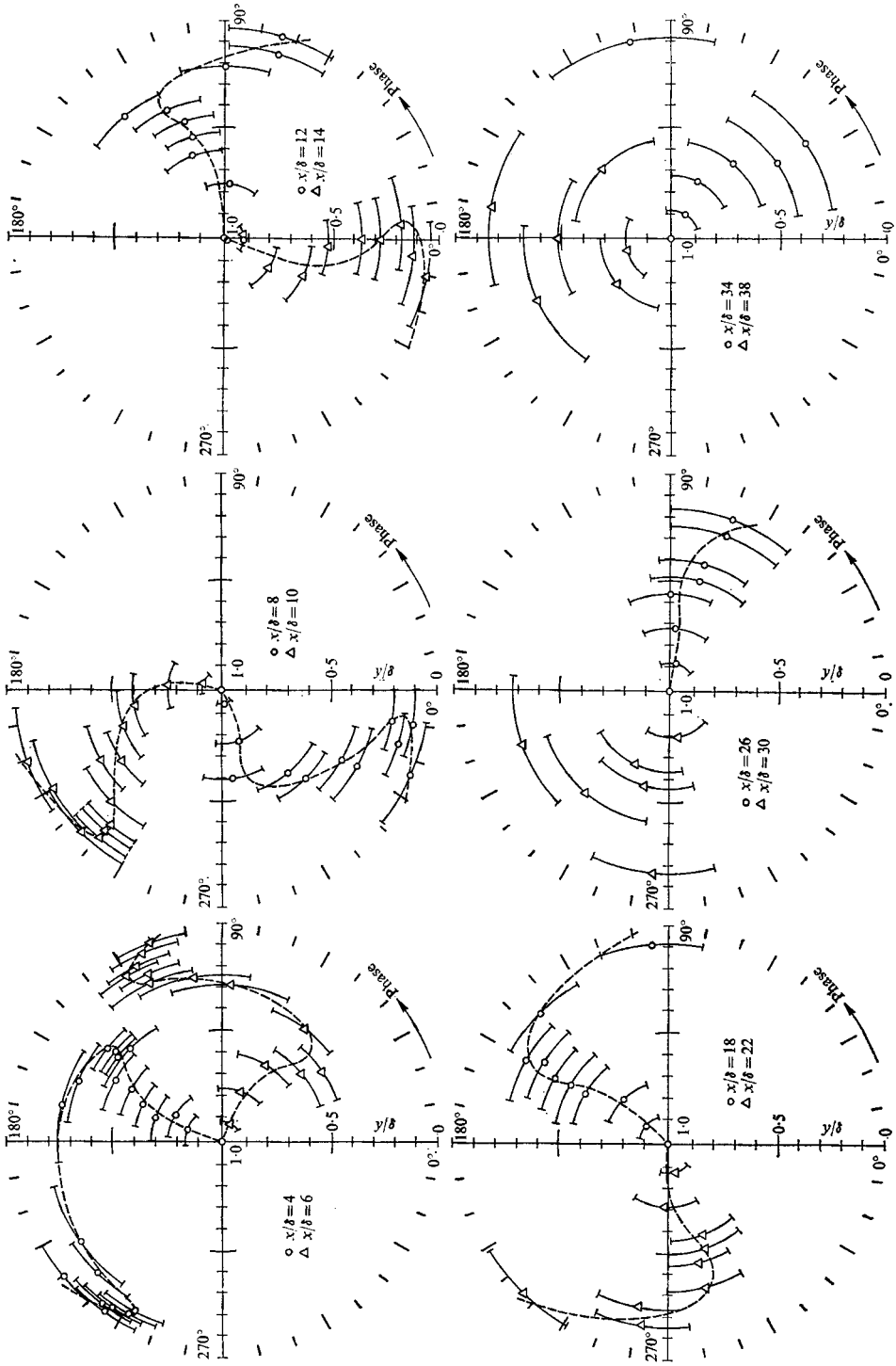

FIGURE 2(*b*). For legend see facing page.

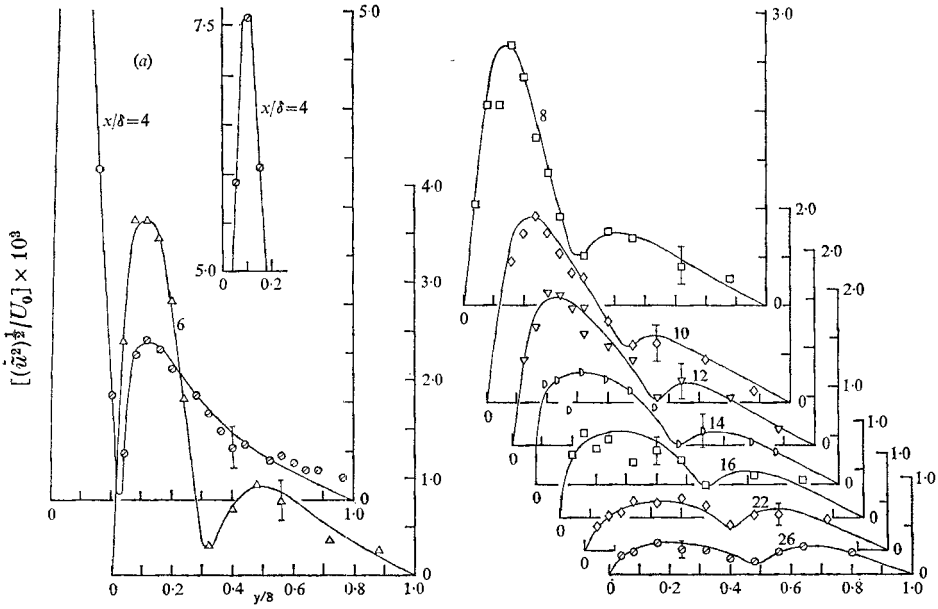

FIGURE 3. Measured (*a*) $\tilde{u}$ amplitude and (*b*) $\tilde{u}$ phase distributions at 50 Hz.

moved so as to produce either symmetric or antisymmetric disturbances in the disturbance velocity field. The ribbon current forms a useful reference signal for analysis of the hot-wire data. Care was taken to maintain a fixed ribbon amplitude for all runs at a given frequency, thus permitting surveys taken on different days to be properly related.

It is convenient to represent the velocity field as a superposition of three components:

$$u_i = \overline{u}_i + \tilde{u}_i + u_i'. \tag{1.1}$$

Here $\overline{u}_i$ is the mean (time-averaged) contribution, $\tilde{u}_i$ is the periodic contribution (the organized wave) and u_i' corresponds to the turbulent motion. Straightforward time-averaging determines $\overline{u}_i$. In order to measure $\tilde{u}_i$ we use a phase-averaging technique (see I); the phase average is defined as the average at a given phase in the cycle of the basic wave (i.e. the reference signal). A wave form eductor, a device which can simultaneously determine the phase average at 100 points in the cycle of the basic wave, is used for this process. The eductor samples the signal at 100 points in each cycle and computes a running average at each of these points. In our experiments the wave component is very weak, so a large ensemble of cycles (typically 10^5) is required. The phase average of the signal then gives the sum of the mean and the organized wave. Denoting the phase average by $\langle\rangle$, we have

$$\langle u_i \rangle = \overline{u}_i + \tilde{u}_i. \tag{1.2}$$

In effect, the phase-averaging process rejects the random background turbulence and extracts the organized motions from the total signal.

A linearized constant-temperature hot-wire anemometer is used to measure the streamwise velocity at selected points downstream of the ribbon. The

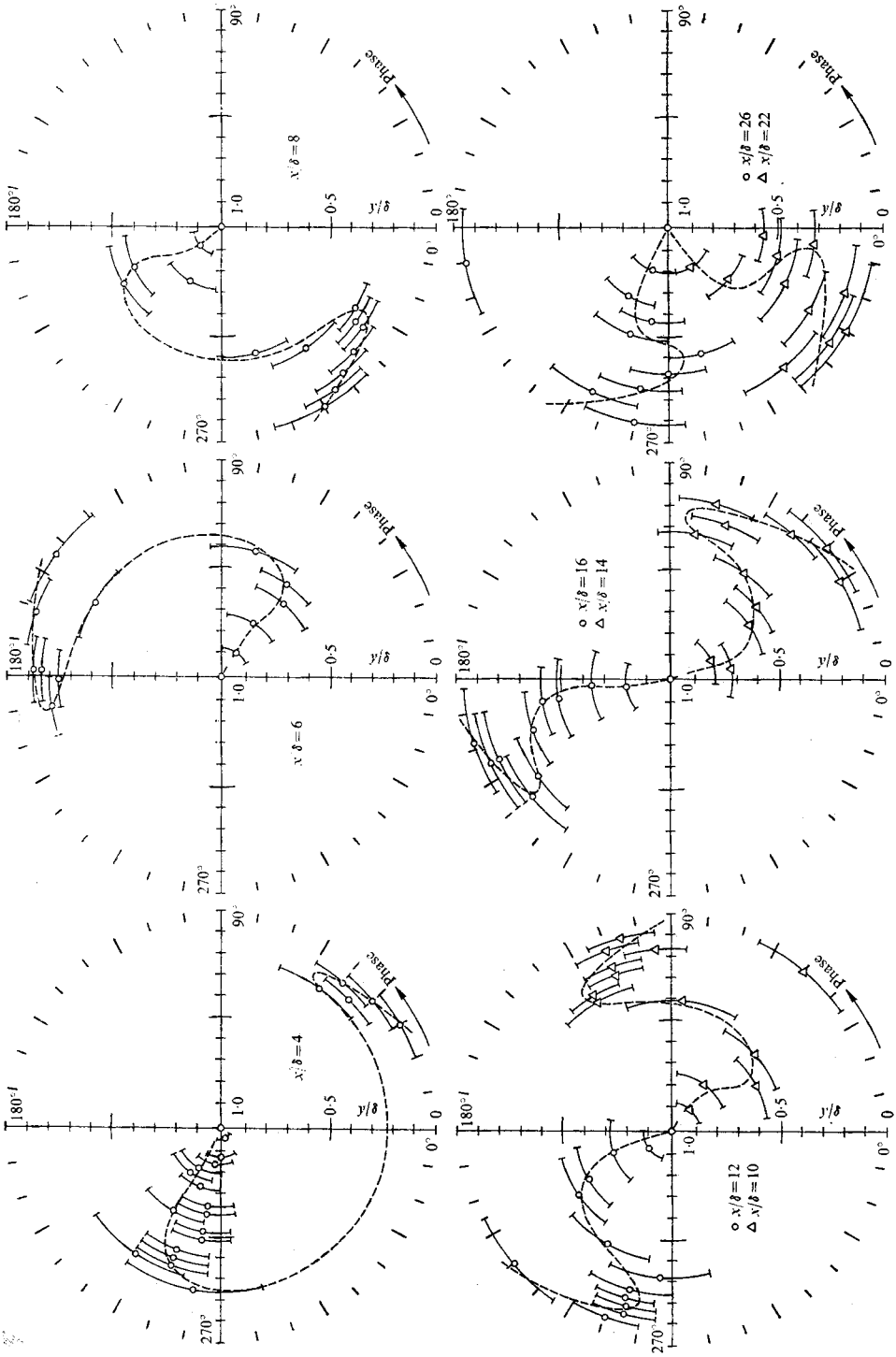

FIGURE 3(*b*). For legend see facing page.

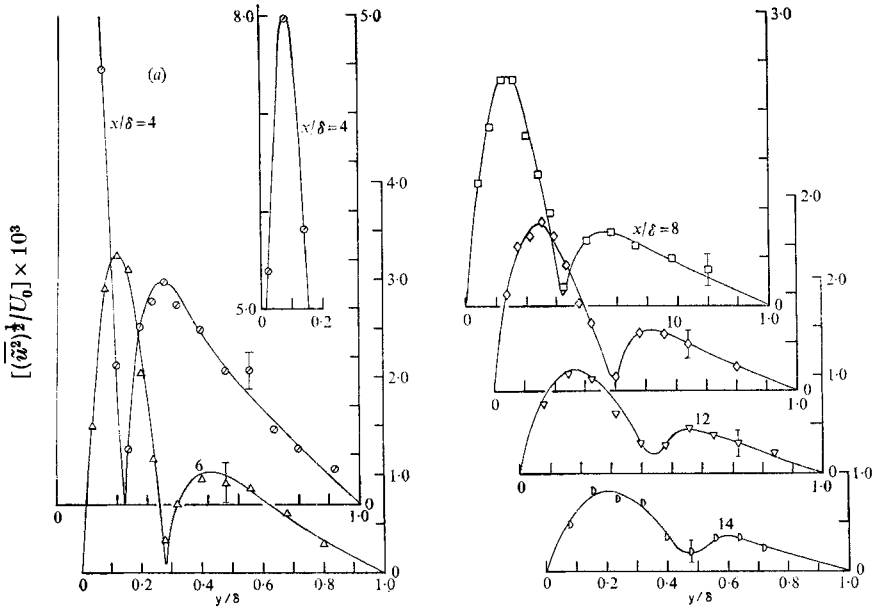

FIGURE 4. Measured (*a*) $\tilde{u}$ amplitude and (*b*) $\tilde{u}$ phase distributions at 75 Hz.

hot-wire signal is first amplified with an a.c. coupled amplifier, which rejects the d.c. component, and the amplified signal is then fed to the wave form eductor, which provides the desired phase-averaged signal as an output. The educed wave form is in general slightly non-sinusoidal, and the sinusoidal component is extracted by analysing the continuous educed signal with a lock-in amplifier. A schematic diagram of the circuitry is given in I; for more details the reader should refer to R.

Suppose that we represent the reference signal (ribbon voltage) by

$$e_r = a\cos(\omega t) \tag{1.3}$$

and the educed hot-wire signal corresponding to the streamwise component $\tilde{u}_1$ at a fixed point by

$$\tilde{u}_1 = |\tilde{u}_1|\cos(\omega t - \phi). \tag{1.4}$$

Then the signal analysis processes outlined above give us both the amplitude $|\tilde{u}_1|$ and phase ϕ of $\tilde{u}_1$ locally.

We denote the distance downstream from the ribbon by x, the distance from one wall by y and the channel half-width by δ (figure 1). All measurements reported here were taken at the channel centre-height ($z = 0$) with a centre-line velocity $U_0 = 21{\cdot}9$ ft/s, corresponding to a Reynolds number $U_0\delta/\nu$ of 13800. Spanwise surveys indicate that the waves remain quite two-dimensional as they progress downstream, hence we have treated the disturbance wave as two-dimensional. For documentation see R.

In I we reported partial data at 100 Hz. Here we report the data for 25, 50, 75 and 100 Hz. For more detail see R.

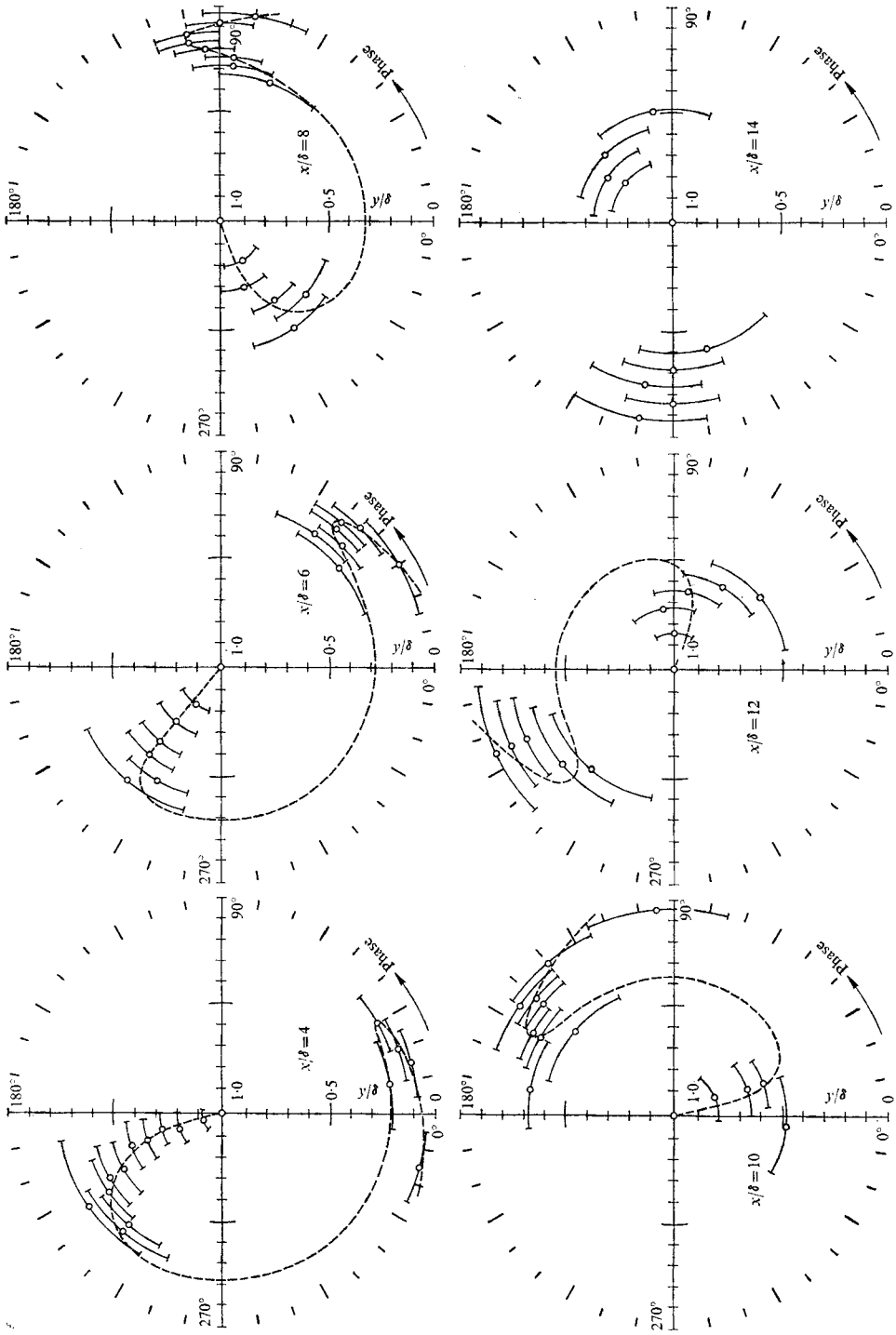

FIGURE 4(*b*). For legend see facing page.

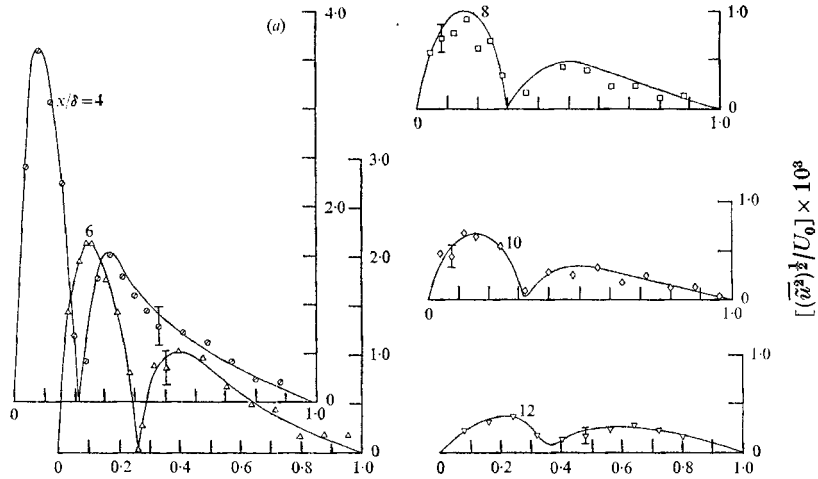

FIGURE 5. Measured (*a*) $\tilde{u}$ amplitude and (*b*) $\tilde{u}$ phase distributions at 100 Hz.

2. Wave data

The data are given in figures 2–5. The phase plots show ϕ *vs.* y/δ at selected streamwise stations x/δ. Note that the origin of these phase plots corresponds to the channel centre-line ($y/\delta = 1$) and that the circumference of the polar plots corresponds to the wall ($y/\delta = 0$). The bars on the data indicate the experimental uncertainty as estimated from selected repetitions of the experiments. These data were taken with the ribbons vibrating in the same direction at the same time; this produces a disturbance which is antisymmetric in the streamwise fluctuation $\tilde{u}$ and symmetric in the cross-stream fluctuation $\tilde{v}$. Surveys in the range

$$1 < y/\delta < 2$$

confirm this antisymmetry in $\tilde{u}$ (see R).

The magnitudes of the amplitudes should be noted. Observe that the r.m.s. disturbance amplitude is typically one-thousandth of the centre-line mean velocity U_0, or a few hundredths of the turbulence r.m.s. velocity. Thus we are able to recover an extremely weak organized component from a background of finite fluctuations.

Let us first concentrate on the amplitude behaviour. In each case the disturbance amplitude generally decreases in the downstream direction, although in some cases there is a momentary increase at particular y positions. By analogy with linear stability theory, one might expect that the amplitude curves would retain their shape, provided of course that the ribbons excite a single disturbance eigenmode. However, there are significant changes in the shapes of the amplitude curves in each case, although in each case there is an apparent tendency towards self-similarity at the most downstream stations. Again calling on stability theory for insight, we recognize that a superposition of several eigenmodes having the same frequency, but each decaying at a different rate in the streamwise direction, would not be self-similar but would approach this behaviour far downstream,

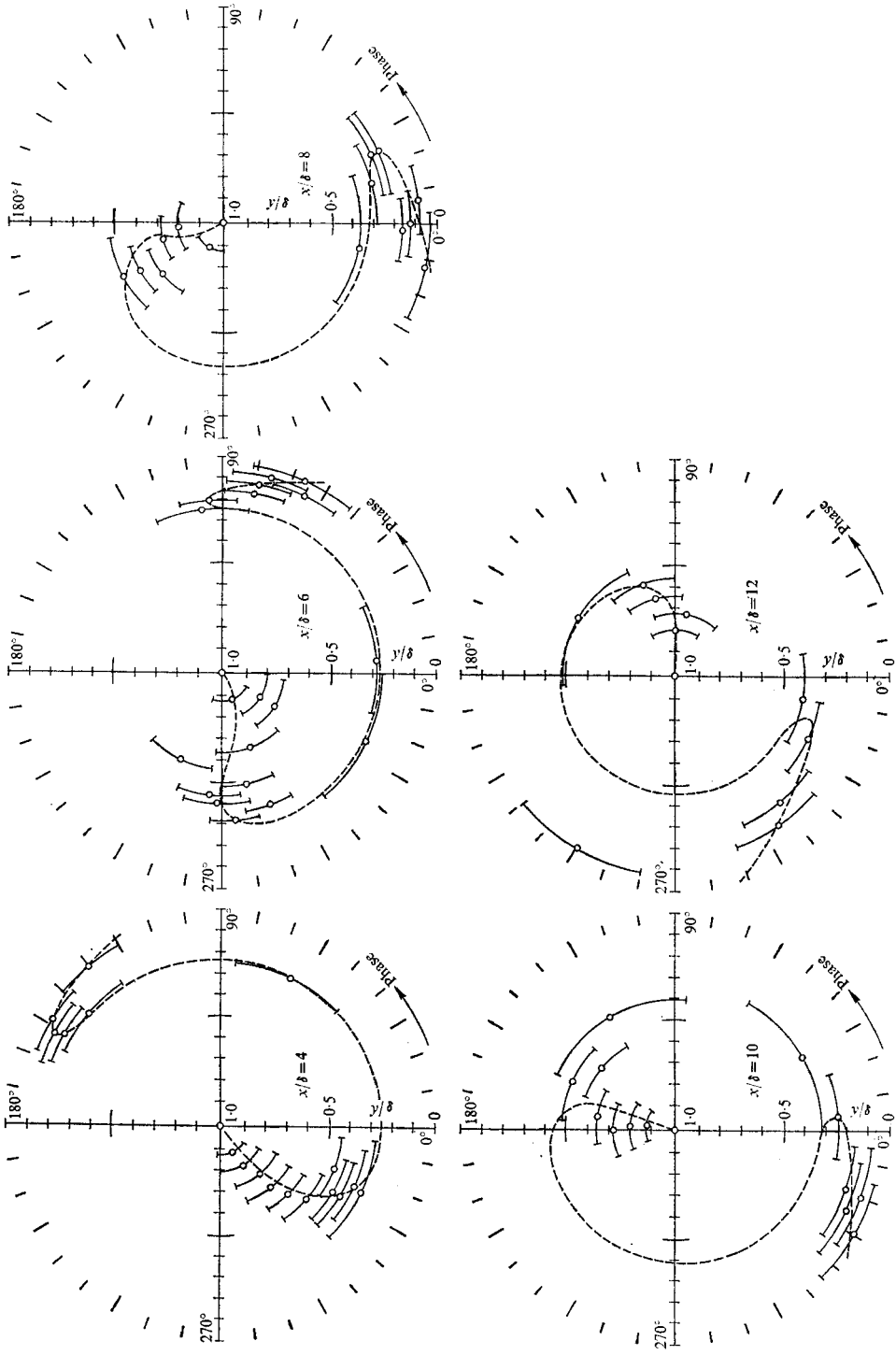

FIGURE 5(*b*). For legend see facing page.

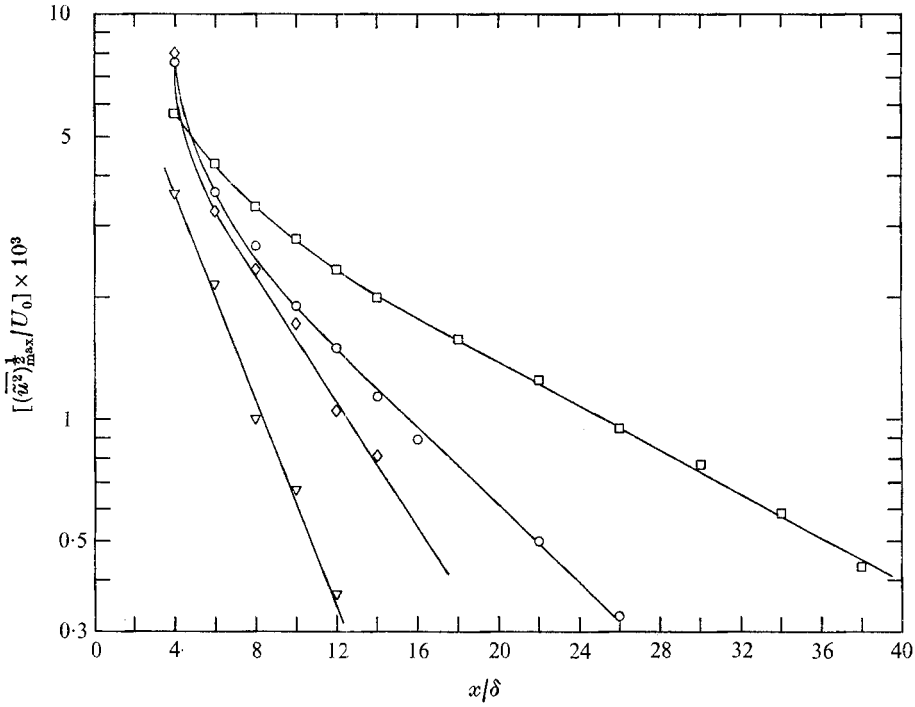

FIGURE 6. Peak of $\tilde{u}$ amplitude at different streamwise stations. $Re = 13800$; □, 25 Hz; ○, 50 Hz; ◇, 75 Hz; ▽, 100 Hz.

where the most slowly decaying mode would dominate. Thus, we should not be surprised to observe changes in the amplitude distribution as the disturbance progresses downstream.

Figure 6 shows the maximum disturbance amplitude as a function of x for the four test frequencies. Note that the streamwise decay is most rapid for the highest frequencies and that the maximum amplitude (which at different x stations occurs at different y points) decays exponentially after an initial region near the ribbon. Exponential decay is indeed the behaviour one would expect from small amplitude disturbance theory, and one therefore suspects that the disturbance should be modelled adequately by a linear theory. Figure 7 shows the streamwise decay at fixed y stations for each of the four frequencies. The dashed line corresponds to an exponential decay for subsequent use in comparing the data with linearized disturbance theories.

The phase distributions (see figures 2(*b*)–5(*b*)) also show a somewhat self-similar nature. The sudden phase change that takes place midway across the flow results from vorticity shed by the oscillating ribbon. In linearized disturbance theories, a normal-mode disturbance will travel downstream with a self-preserving phase distribution, offset by an angle related to the disturbance propagation speed. Since the data determine the phase angle only within $0° \leqslant \phi \leqslant 360°$, some interpretation is needed to relate properly the phases at two streamwise stations. By giving due consideration to the probable magnitude of the disturbance propagation velocity (see §3 for more detail) we arrived at the

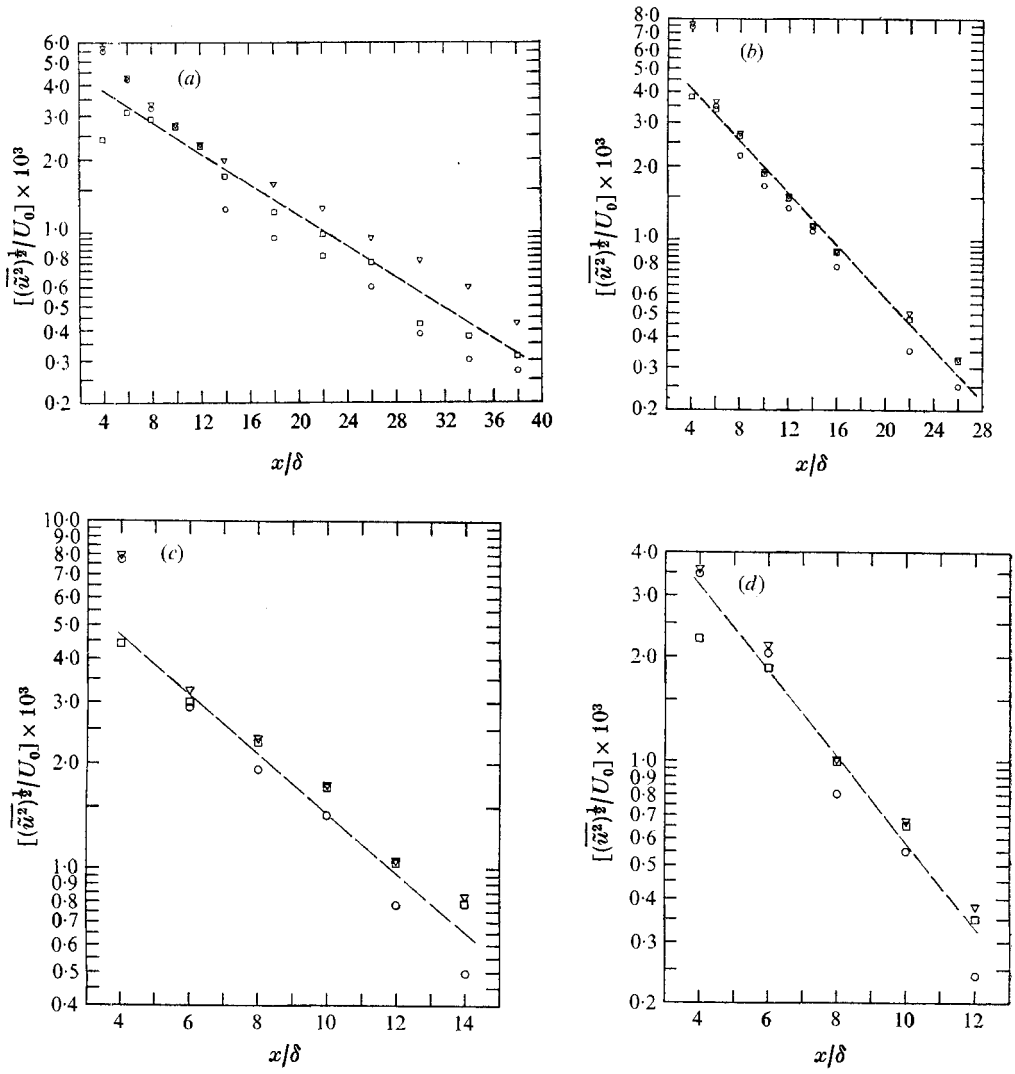

FIGURE 7. Wave amplitude decay estimates. ▽, peak; ○, $y = 0{\cdot}1$ in.; □, 0·2; – – –, average interpretation. (*a*) 25 Hz. (*b*) 50 Hz. (*c*) 75 Hz. (*d*) 100 Hz.

related phase distributions shown, for two y stations, in figure 8. Note that the phase advances most slowly for the lowest frequency disturbance. The linearity of these curves strongly suggests a constant disturbance propagation velocity, as would be expected from a linearized disturbance theory.

Some insight as to the presence of higher harmonics in the educed signal was obtained from oscillascope pictures taken at each point. These pictures also provided a convenient visual check on the measured amplitudes and phases, and on the stability of the educed pattern. The higher harmonics are important only very near the ribbon; in the region where exponential decay is observed they seem unimportant. For photographs and Fourier analyses of particular wave forms see R.

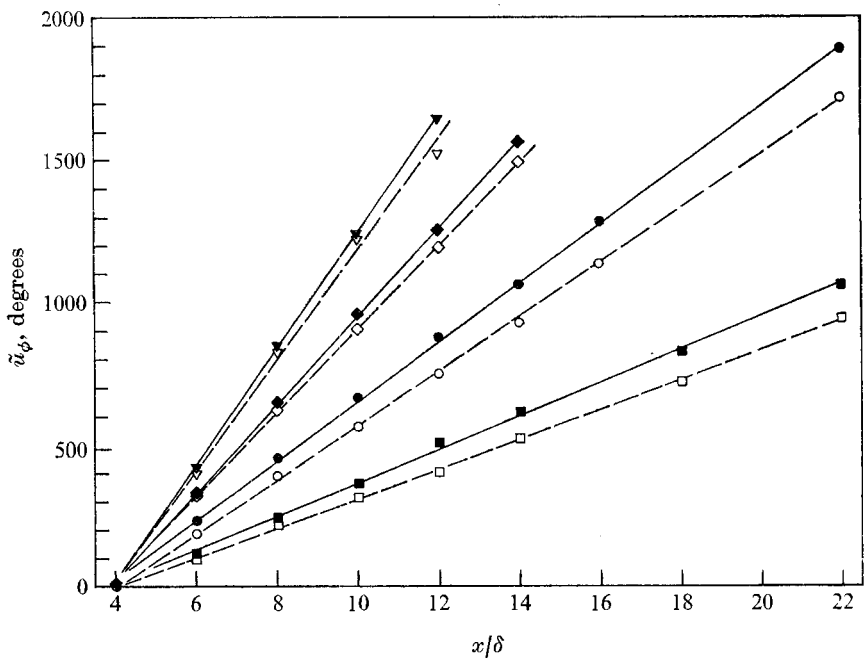

FIGURE 8. Phases of $\tilde{u}$ at constant distance from the wall.

	100 Hz	75 Hz	50 Hz	25 Hz
$y/\delta = 0{\cdot}16$	▼	◆	●	■
$y/\delta = 0{\cdot}56$	▽	◇	○	□

3. Single-mode analysis

From the discussion above it is clear that the disturbance wave shapes are not exactly preserved in the streamwise direction, and hence the disturbance waves are not pure modes. A proper analysis of the data will therefore require a multiple-mode analysis. However, for the purpose of approximate analysis of the data and evaluation of average propagation characteristics, the disturbance will now be treated as though it were exactly a single mode. It is also assumed that the wave amplitudes are sufficiently small to be treated by linear theory. All quantities will be treated as dimensionless, using the channel half-width δ and the centre-height ($z = 0$) continuity velocity U_m as the reference scales. Note that for this flow $U_m/U_0 = 0{\cdot}881$, where U_0 is the velocity on the channel centre-line.

It is usual to represent the two-dimensional normal-mode perturbation wave as

$$\tilde{\mathbf{u}}(x,y,t) = \tfrac{1}{2}\{\hat{\mathbf{u}}(y)\,e^{i\alpha(x-ct)} + \hat{\mathbf{u}}^*(y)\,e^{-i\alpha^*(x-c^*t)}\}. \tag{3.1a}$$

where * denotes a complex conjugate, $\hat{\mathbf{u}}(y) = [\hat{u}(y), \hat{v}(y), 0]$ is the two-dimensional complex eigenmode shape, $\alpha = \alpha_r + i\alpha_i$ is the (complex) wavenumber, α_r being the streamwise wavenumber and α_i the growth factor, and $c = c_r + ic_i$ is the (complex) wave speed. Alternatively, one may write (3.1a) as

$$\tilde{\mathbf{u}} = \tfrac{1}{2}\{\hat{\mathbf{u}}(y)\,e^{i(\alpha x-\omega t)} + \text{conjugate}\}, \tag{3.1b}$$

	25 Hz	50 Hz	75 Hz	100 Hz
$\Delta\phi/\Delta x$	$56 \pm 7°$	$107 \pm 9°$	$156 \pm 11°$	$204 \pm 12°$
α_r	$0{\cdot}981 \pm 13\,\%$	$1{\cdot}87 \pm 8{\cdot}5\,\%$	$2{\cdot}72 \pm 7\,\%$	$3{\cdot}57 \pm 6{\cdot}1\,\%$
α_i	$0{\cdot}0727 \pm 10\,\%$	$0{\cdot}122 \pm 12\,\%$	$0{\cdot}196 \pm 14\,\%$	$0{\cdot}285 \pm 16\,\%$
ω	0·847	1·692	2·54	3·39
c_r	$0{\cdot}861 \pm 13\,\%$	$0{\cdot}904 \pm 8{\cdot}5\,\%$	$0{\cdot}93 \pm 7\,\%$	$0{\cdot}946 \pm 6{\cdot}1\,\%$
c_i	$-0{\cdot}0638 \pm 10\,\%$	$-0{\cdot}0591 \pm 12\,\%$	$-0{\cdot}0672 \pm 14\,\%$	$-0{\cdot}0755 \pm 16\,\%$
λ	6·40	3·36	2·31	1·76
V_c	0·862	0·905	0·934	0·949
a	0·465	0·420	0·451	0·501

TABLE 1. Wave data. All quantities are dimensionless and normalized using δ and U_m; $U_0\delta/\nu = 13800$, $U_m/U_0 = 0{\cdot}881$.

where ω is the (real) circular frequency of the oscillation. Note that

$$c = \omega/\alpha. \tag{3.2}$$

The actual wave phase velocity is

$$V_c \equiv \omega/\alpha_r. \tag{3.3}$$

Within the approximation mentioned above, it is possible to estimate the propagating wave characteristics (α_r, α_i, c_r and c_i) from the data. For two stations x_1 and x_2, both at the same distance y from the wall,

$$|\tilde{u}(x_2, y, t)|/|\tilde{u}(x_1, y, t)| = e^{-\alpha_i(x_2 - x_1)}. \tag{3.4}$$

Hence

$$\alpha_i = \frac{\ln(|\tilde{u}_1|/|\tilde{u}_2|)}{(x_2 - x_1)}. \tag{3.5}$$

Values of α_i as obtained from the average decay estimates shown in figure 7 are given in table 1. Positive values of α_i, as found in this experiment, are qualitatively consistent with the decaying-wave model of Landahl (1967) and the wall-pressure correlation measurements of Willmarth & Wooldridge (1962) and Bull (1963) on a flat plate and Corcos (1964) in a pipe.

From (3.1) it also follows that

$$\tilde{u}(x_2, y, t)/\tilde{u}(x_1, y, t) = \exp[-\alpha_i(x_2 - x_1) + i\alpha_r(x_2 - x_1)]. \tag{3.6}$$

If the phase of $\tilde{u}$ is denoted by ϕ, (3.6) gives

$$\phi(x_2, y, t) = \phi(x_1, y, t) + \alpha_r(x_2 - x_1) \tag{3.7}$$

and thus

$$\alpha_r = (\phi_2 - \phi_1)/(x_2 - x_1). \tag{3.8}$$

Values of α_r deduced from the phase data as interpreted in figure 8 are given in table 1.

Once α_r and α_i are known, c can be calculated from (3.2) and V_c from (3.3). Also of interest are the wavelength

$$\lambda = 2\pi/\alpha_r \tag{3.9}$$

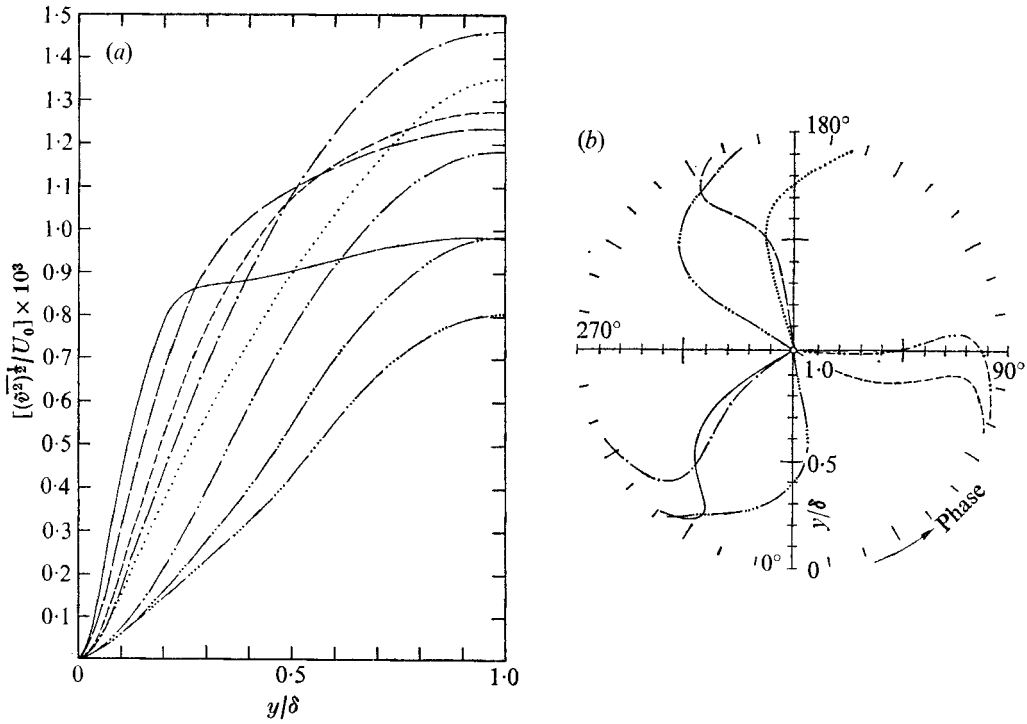

FIGURE 9. Inferred (*a*) $\tilde{v}$ amplitude and (*b*) $\tilde{v}$ phase distributions at 25 Hz. —, $x/\delta = 4$; – –, $x/\delta = 6$; - - - -, $x/\delta = 8$; — · —, $x/\delta = 10$; · · · · · ·, $x/\delta = 12$; — · · —, $x/\delta = 14$; — · · · —, $x/\delta = 18$; — · · · · —, $x/\delta = 22$.

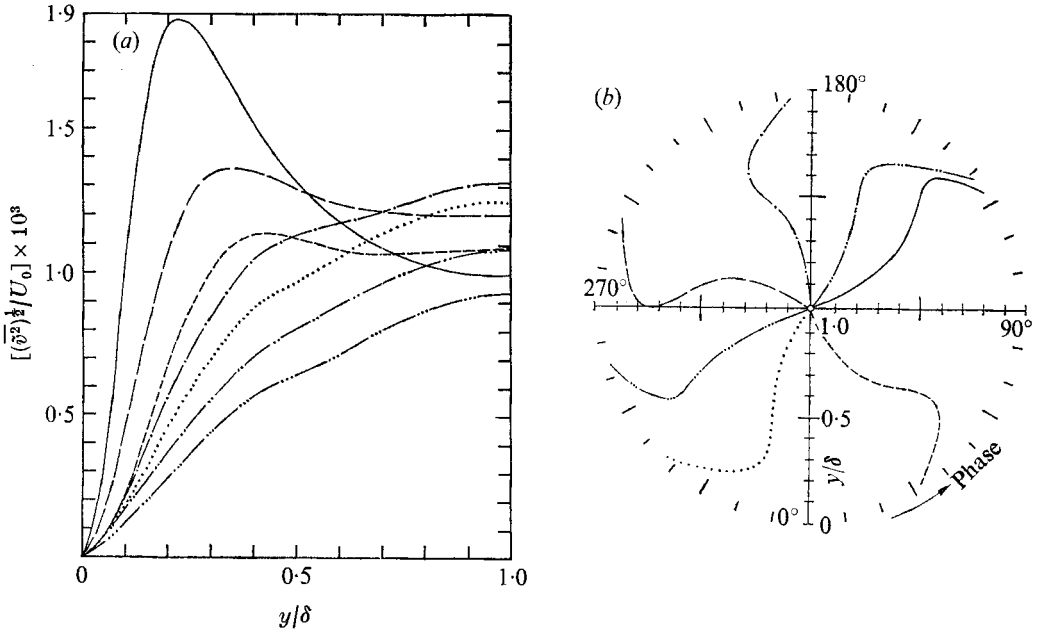

FIGURE 10. Inferred (*a*) $\tilde{v}$ amplitude and (*b*) $\tilde{v}$ phase distributions at 50 Hz. Notation as in figure 9.

and the attenuation factor per wavelength,

$$a = \alpha_i \lambda. \tag{3.10}$$

Values of c, V_c, λ and a are also included in table 1.

Two features of the data deserve comment. First, we note that the convection velocity increases slightly with frequency over the range investigated. Second, the attenuation per wavelength is, within the experimental uncertainty, *independent* of the frequency, with $\alpha_i/\alpha_r \approx 0{\cdot}07$ over the range of frequencies investigated.

Some additional remarks on the determination of the phase differences may be helpful. In the polar phase diagrams (figures 2(*b*)–5(*b*)) one can read the phase difference between stations clockwise or counterclockwise, and in each case one can also add or subtract multiples of 360°. To understand how we unravelled this riddle, consider figure 2(*b*) and concentrate on the phase distribution at stations $x/\delta = 8, 10, 12$ and 14. The distributions are similar, the phase difference between two successive stations being about 120° clockwise. The corresponding phase velocity from (3.3) is $V_c = 0{\cdot}81$. If the angle is instead taken counterclockwise, i.e. as 240°, we have $V_c = 0{\cdot}405$. If 360° were added in clockwise direction we would obtain $V_c = 0{\cdot}2$, and if 360° were added in the counterclockwise direction $V_c = 0{\cdot}16$. It seems reasonable that these large-scale disturbances travel at a speed close to the channel mean speed (which corresponds to $V_c = 1$), hence the clockwise interpretation giving a phase difference of about 120° is selected.

The above comparisons lead one to favour strongly the measurement of phase between stations in the clockwise direction. Once this has been decided upon, the same system is followed for other frequencies. In this way the angles measured for 50 Hz and 75 Hz are approximately 215° and 310° respectively. However, at 100 Hz the clockwise direction measurement has to be carried out in a slightly different way to keep the angles consistent. In this case an extra 360° must be added while measuring the phase difference between two successive stations. This yields an average phase difference between two stations of about 410° and a corresponding phase velocity $V_c = 0{\cdot}94$. Without this addition of 360° the angle is only 50° and the corresponding phase velocity would be $V_c = 0{\cdot}078$.

For a two-dimensional disturbance the continuity equation is

$$\partial\tilde{u}/\partial x + \partial\tilde{v}/\partial y = 0. \tag{3.11}$$

Now, in the single-mode analysis,

$$\partial\tilde{u}/\partial x = i\alpha\hat{u}\, e^{i\alpha x - i\omega t} + \text{conjugate}. \tag{3.12}$$

Using this in (3.11), and writing

$$\tilde{v} = \hat{v}(x, y)\, e^{-i\omega t} + \text{conjugate}, \tag{3.13}$$

we have

$$\hat{v}(x, y) = -i\alpha \int_{\sigma}^{y} \hat{u}(x, y_1)\, dy_1. \tag{3.14}$$

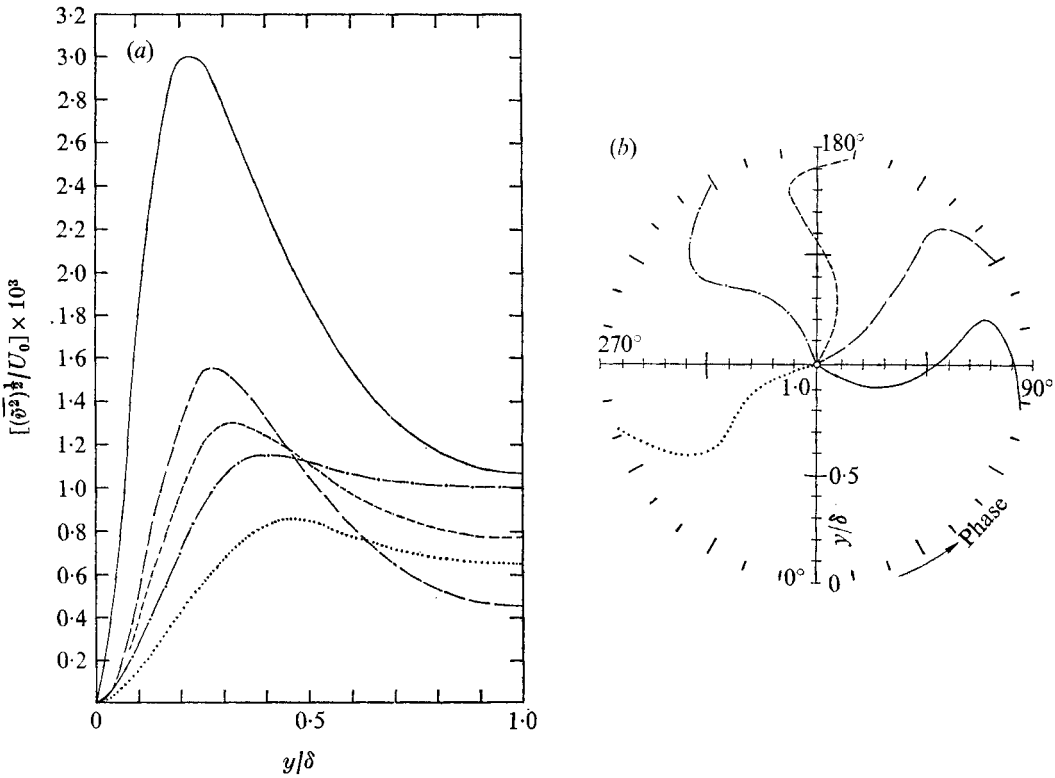

FIGURE 11. Inferred (*a*) $\tilde{v}$ amplitude and (*b*) $\tilde{v}$ phase distributions at 75 Hz. Notation as in figure 9.

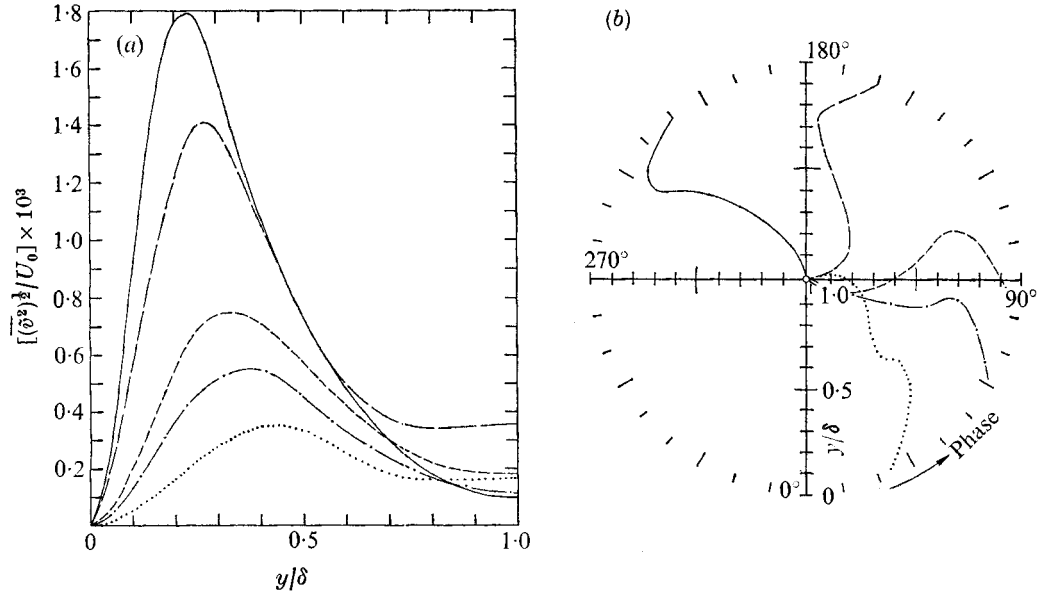

FIGURE 12. Inferred (*a*) $\tilde{v}$ amplitude and (*b*) $\tilde{v}$ phase distributions at 100 Hz. Notation as in figure 9.

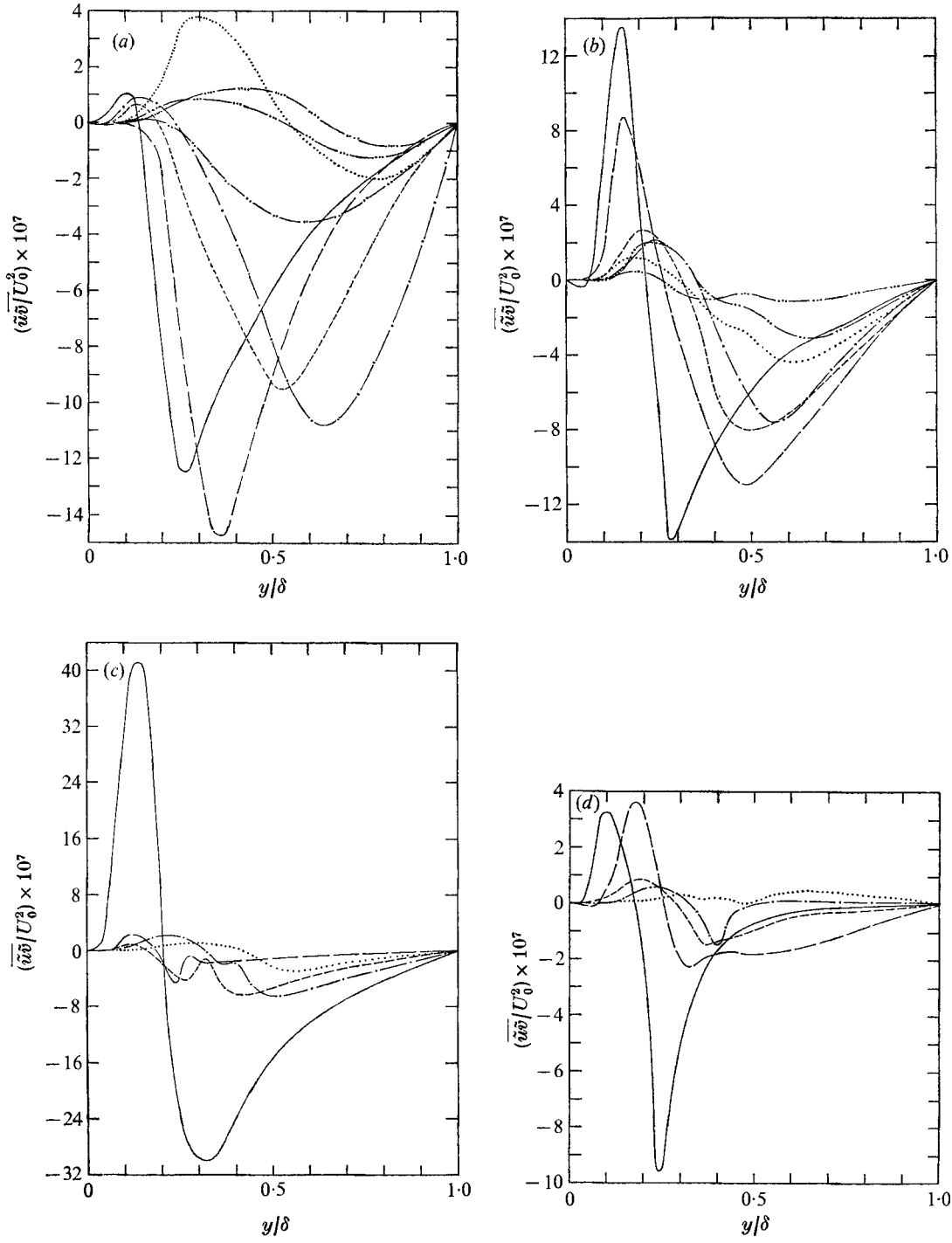

FIGURE 13. Inferred $\overline{\tilde{u}\tilde{v}}$ distribution. (*a*) 25 Hz, (*b*) 50 Hz, (*c*) 75 Hz and (*d*) 100 Hz. Notation as in figure 9.

Although one should be careful not to take the calculation too seriously, we did compute $\tilde{v}$ using (3.14) and smoothed curves through the measured $\tilde{u}$ data; the results are shown in figures 9–12. The striking feature is the apparent peakiness of $\tilde{v}$ near the wall for the higher frequency disturbances. This is, indeed, quite similar to the behaviour obtained from solutions of the Orr–Sommerfeld equation for small amplitude disturbances on a laminar shear flow. Note that the $\tilde{v}$ curves are not self-similar near the ribbon but seem to be progressing towards a self-similar shape in the downstream direction. This would be characteristic of a disturbance formed from a superposition of a lightly damped and a more heavily damped eigenmode.

Armed with both $\tilde{u}$ and $\tilde{v}$ data, one might be tempted to compute the disturbance Reynolds stress distribution. In view of the problems arising from a one-mode treatment, one should yield to this temptation only after issuing a considerable warning to the readers, which is implicit in this discussion. The wave Reynolds stress is

$$\overline{\tilde{u}\tilde{v}} = \tfrac{1}{4}(\hat{u}\hat{v}^* + \hat{u}^*\hat{v}). \tag{3.15}$$

Having cautioned fiercely against substantiative use of these results, we note that the wave Reynolds stresses are given in figure 13.

It should be clear that a direct measurement of $\tilde{v}$ would be preferable to the calculations outlined above. In addition to those of the wave Reynolds stress, one would also like to have direct measurements of the wave-induced fluctuations in the turbulent Reynolds stresses:

$$\tilde{r}_{ij} \equiv \langle u_i' u_j' \rangle - \overline{u_i' u_j'}. \tag{3.16}$$

Such measurements are now in progress at Stanford.

4. Relationships to 'natural' flows

In attempting to compare these data with parameters deduced from various filtered correlation data obtained in 'natural' (undisturbed) flows, two points must be kept in mind. First, the typical filtered correlation measurements (e.g. Wills 1964) include contributions from waves of all obliquities, not just the two-dimensional waves. Second, the waves studied here are relatively long in comparison with those studied in most previous experiments. These facts make comparisons with most previous data very difficult. However, Landahl (1967) pointed out that Corcos's (1964) wall-pressure data indicate that the wall-pressure cross-power spectral density is dominated by waves that are nearly normal to the stream. Consequently, it does make some sense to compare our two-dimensional wave data to such pressure data. Although the data for boundary layers are more extensive, comparison with pipe flows seems more reasonable, and we shall use Corcos's (1964) pipe data for this comparison.

One of the most striking observations in Corcos's data, also observed by Willmarth & Wooldridge (1962), is that the amplitude of the wall-pressure cross-power spectral density depends only upon the parameter $\omega\xi/V_c$, where ξ is the separation distance in the streamwise direction. In figure 14 we have replotted

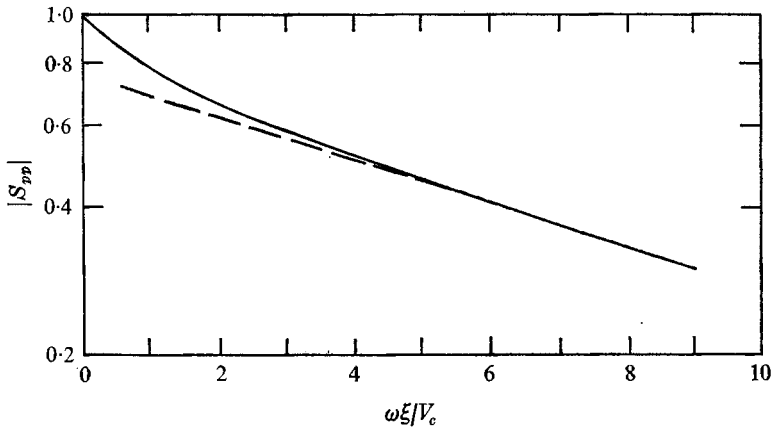

FIGURE 14. Comparison of wall-pressure cross-power spectral density. —, Corcos's data; – – –, equation (4.7).

Corcos's data on semi-log paper; the striking similarity with figure 6 should be noted. For long separation distances the behaviour is essentially exponential, which is consistent with our small-disturbance model.

If we view the turbulence in a pipe as being composed of a superposition of weak waves and assume that the pressure will be dominated by long two-dimensional waves of the type studied here, a direct quantitative comparison can be made. We represent the contribution of a single wave to the wall pressure by

$$\tilde{p} = \hat{p}_w^n \exp\{-\alpha_i^n x + i\alpha_r^n x + i\omega t\} + \text{conjugate}. \tag{4.1}$$

Here the superscript n denotes the nth wave. It seems reasonable to assume that the waves are uncorrelated, i.e. that

$$\langle \hat{p}_w^n \hat{p}_w^{*m} \rangle = A_n \delta_{nm}. \tag{4.2}$$

Here $\langle\ \rangle$ denotes an ensemble average. Then the autocorrelation of the wall pressure is

$$\begin{aligned} R_{pp} &= \overline{\langle p_w(x,t) p_w(x+\xi, t+\tau)\rangle} \\ &= \sum_n |A_n|^2 \exp\{-2\alpha_i^n x - \alpha_i^n \xi - i\alpha_r^n \xi - i\omega^n \tau\} + \text{conjugate}. \end{aligned} \tag{4.3}$$

Now, the harmonic decomposition with respect to τ defines the cross-power spectral density. We see that the amplitude of the cross-power spectral density should behave like (see Landahl 1967)

$$|S_{pp}(\omega)| \sim \sum_n |A_n|^2 e^{-\alpha_i^n \xi}. \tag{4.4}$$

This may be written as

$$|S_{pp}(\omega)| \sim \sum_n |A_n|^2 \exp\left\{-\frac{\alpha_i^n}{\alpha_r^n}\alpha_r^n \xi\right\} \tag{4.5}$$

or, using (3.3),

$$|S_{pp}(\omega)| \sim \sum_n |A_n|^2 \exp\left\{-\frac{\alpha_i^n}{\alpha_r^n}\frac{\omega^n \xi}{V_c}\right\}. \tag{4.6}$$

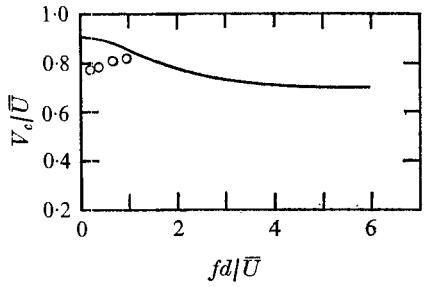

FIGURE 15. Comparison of convection velocities for with Corcos's data for pipe flow. —, Corcos's data based on wall pressures; ○, present data.

The experiments deal with the 'least-damped' modes, which of course will dominate $|S_{pp}|$ for large ξ. For these modes we find $\alpha_i/\alpha_r = 0{\cdot}07$, and hence for large ξ we would expect $|S_{pp}|$ to depend only upon the parameter $\omega\xi/V_c$, as indeed is found experimentally. For large ξ the least-damped mode should dominate, and hence we would expect

$$|S_{pp}| \sim \text{constant} \times \exp\{-0{\cdot}07\omega\xi/V_c\} \quad \text{as} \quad \xi \to \infty. \tag{4.7}$$

The dashed line in figure 14 shows this asymptotic behaviour, which is in remarkable agreement with Corcos's data.

Corcos also measured the convection velocity of the wall-pressure disturbances. If we again assume that the two-dimensional waves dominate the wall pressure, then a comparison can be made. Figure 15 shows Corcos's data; f is the frequency (Hz), d is the pipe diameter and $\overline{U}$ is the 'mean discharge velocity' for the pipe. Using 2δ instead of d and U_m for $\overline{U}$, the present data are also shown. Note that the present experiments are confined to relatively low frequencies and that values comparable with Corcos's are found, although the trends with frequency seem to be in opposite directions. This might be due to dominance of more strongly oblique waves at the higher frequencies.

The close association between our data for two-dimensional waves and Corcos's wall-pressure data provides considerable support for the notion that it is useful to view shear-flow turbulence as waves (Landahl 1967).

5. Concluding remarks

The results given here provide the first real means of testing model equations purporting to describe the behaviour of wavelike disturbances in a turbulent shear flow. Although the $\tilde{u}$ data are reported with some confidence, the inferred $\tilde{v}$ data should be used with caution, pending direct experimental measurement. The work described in this paper is now being extended at Stanford using a better technique (cross-correlation) for sifting out the periodic component of the hot-wire signal, and in due course we shall be able to provide theoreticians with good measurements of both the wave components $\tilde{u}_1$ and the wave-induced Reynolds stress fluctuations $\tilde{r}_{ij}$ for a well-documented turbulent channel flow.

Additional interpretation of these data, in relationship to pending theoretical models, is given in part 3 of this investigation (Reynolds & Hussain 1972).

This work is sponsored by the Mechanics Branch of the Air Force Office of Scientific Research and by the National Science Foundation; their assistance is gratefully acknowledged.

REFERENCES

BULL, M. K. 1963 Properties of the fluctuating wall-pressure field of a turbulent boundary layer. *University of Southampton A.A.S.U. Rep.* no. 234.

CORCOS, G. M. 1964 *J. Fluid Mech.* **18**, 353.

HUSSAIN, A. K. M. F. & REYNOLDS, W. C. 1970*a* *J. Fluid Mech.* **41**, 241.

HUSSAIN, A. K. M. F. & REYNOLDS, W. C. 1970*b* The mechanics of a perturbation wave in turbulent shear flow. *Department of Mechanical Engineering Rep., Stanford University*, FM-6.

LANDAHL, M. T. 1967 *J. Fluid Mech.* **29**, 441.

REYNOLDS, W. C. & HUSSAIN, A. K. M. F. 1972 *J. Fluid Mech.* **54**, 263.

WILLMARTH, W. W. & WOOLDRIDGE, C. E. 1962 *J. Fluid Mech.* **11**, 187.

WILLS, J. A. B. 1964 *J. Fluid Mech.* **20**, 417.